

# On the universality of luminosity-metallicity and mass-metallicity relations for compact star-forming galaxies at redshifts $0 < z < 3$

Y. I. Izotov<sup>1,2,3</sup>, N. G. Guseva<sup>1,2</sup>, K. J. Fricke<sup>2,4</sup> and C. Henkel<sup>2,5</sup>

<sup>1</sup>*Main Astronomical Observatory, Ukrainian National Academy of Sciences, Zabolotnoho 27, Kyiv 03680, Ukraine*

<sup>2</sup>*Max-Planck-Institut für Radioastronomie, Auf dem Hügel 69, 53121 Bonn, Germany*

<sup>3</sup>*LUTH, Observatoire de Paris, CNRS, Université Paris Diderot, Place Jules Janssen 92190 Meudon, France*

<sup>4</sup>*Institut für Astrophysik, Göttingen Universität, Friedrich-Hund-Platz 1, 37077 Göttingen, Germany*

<sup>5</sup>*Astronomy Department, King Abdulaziz University, P.O. Box 80203, Jeddah 21589, Saudi Arabia*

Accepted 1988 December 15. Received 1988 December 14; in original form 1988 October 11

## ABSTRACT

We study relations between global characteristics of low-redshift ( $0 < z < 1$ ) compact star-forming galaxies, including absolute optical magnitudes,  $H\beta$  emission-line luminosities (or equivalently star-formation rates), stellar masses, and oxygen abundances. The sample consists of 5182 galaxies with high-excitation H II regions selected from the SDSS DR7 and SDSS/BOSS DR10 surveys adopting a criterion  $[O III]\lambda 4959/H\beta \geq 1$ . These data were combined with the corresponding data for high-redshift ( $2 \lesssim z \lesssim 3$ ) star-forming galaxies. We find that in all diagrams low- $z$  and high- $z$  star-forming galaxies are closely related indicating a very weak dependence of metallicity on stellar mass, redshift, and star-formation rate. This finding argues in favour of the universal character of the global relations for compact star-forming galaxies with high-excitation H II regions over redshifts  $0 < z < 3$ .

**Key words:** galaxies: fundamental parameters – galaxies: dwarf – galaxies: starburst – galaxies: ISM – galaxies: abundances.

## 1 INTRODUCTION

Luminosities, stellar masses, and metallicities are among the most important properties of galaxies, which are needed for a better understanding of their formation and evolution. The  $H\beta$  emission-line luminosity allows for a direct measure of the rate of gas transformation into stars, while stellar mass and metallicity are indicators of the galaxy’s past evolution. Thus, relations between these parameters and their variations with redshift may help to analyse the origin and evolution of galaxy populations on cosmological time scales.

In this respect, the study of star-forming galaxies plays a particularly important role. The brightness of these galaxies is enhanced by the ongoing star-formation, allowing us to observe them at larger distances. Furthermore, stronger emission lines in spectra of these galaxies better constrain their metallicity, one of the key galaxy global parameters.

The Sloan Digital Sky Survey (SDSS) imaging and spectroscopy (York et al. 2000) opened a unique opportunity to produce the luminosity-metallicity and mass-metallicity relations for large samples of low- $z$  normal and star-forming galaxies. Tremonti et al. (2004) obtained a mass-metallicity relation for  $\sim 53000$  SDSS star-forming galaxies at  $z \sim 0.1$ .

They found that the relation is relatively steep for low-mass galaxies with stellar masses  $M_* < 10^{10.5} M_\odot$ , but flattens for higher-mass galaxies. The mass-metallicity relation by Tremonti et al. (2004) is often used as a benchmark for comparisons with similar relations obtained for low- $z$  and high- $z$  galaxies (e.g. Lee et al. 2006; Maiolino et al. 2008; Amorín et al. 2010; Manucci et al. 2010; Maier et al. 2014; Steidel et al. 2014; Zahid et al. 2011, 2012, 2013, 2014a,b). However, we note that Tremonti et al. (2004) selected all star-forming galaxies, including galaxies with low-excitation H II regions, while only galaxies with high-excitation H II regions are present in high- $z$  samples. They also used calibrations by Charlot & Longhetti (2001) for the metallicity determination, which were not used for high- $z$  galaxies. This implies that differences between low- $z$  and high- $z$  galaxies can be introduced, at least in part, by different selection criteria and different methods used for the determination of global galaxy parameters such as metallicities and stellar masses.

Maiolino et al. (2008) found a strong evolution of the stellar mass-metallicity relation with redshift in the sense that high- $z$  ( $z \sim 3.5$ ) galaxies are more metal-poor com-

pared to low- $z$  galaxies for the same stellar mass. This effect is more pronounced for low-mass galaxies. Manucci et al. (2010) considered a more general relation between stellar mass  $M_*$ , metallicity, and star-formation rate (SFR). They found that high- $z$  galaxies are characterised by progressively higher SFRs. Introducing a parameter  $\mu = \log M_*/M_\odot - \alpha \log \text{SFR}(M_\odot \text{yr}^{-1})$ , Manucci et al. (2010) showed that, independent of redshift, star-forming galaxies have a uniform  $\mu$  – metallicity distribution if  $\alpha = 0.32$ .

On the other hand, there is some evidence that properties of nearby and high- $z$  star-forming galaxies are similar with respect to SFR and metallicity. Heckman et al. (2005) have identified nearby ( $z < 0.3$ ) ultraviolet-luminous galaxies (UVLGs) selected from the *Galaxy Evolution Explorer* (GALEX). These compact UVLGs were eventually called Lyman-break analogues (LBAs). They resemble LBGs in several respects, implying that mass-metallicity relations for low- $z$  and high- $z$  galaxies should be similar. In particular, their metallicities are subsolar, and their SFRs of  $\sim 4 - 25 M_\odot \text{yr}^{-1}$  are overlapping with those for LBGs.

Furthermore, Cardamone et al. (2009) selected a sample of compact strongly star-forming galaxies from the SDSS, which are also similar to LBGs because of their low metallicities and high SFRs. Izotov et al. (2011) extracted a sample of star-forming luminous compact galaxies (LCGs) with hydrogen  $H\beta$  luminosities  $L(H\beta) \geq 3 \times 10^{40} \text{ erg s}^{-1}$  and  $H\beta$  equivalent widths  $\text{EW}(H\beta) \geq 50 \text{ \AA}$  from SDSS spectroscopic data. These galaxies have properties similar to “green pea” galaxies (Cardamone et al. 2009) but are distributed over a wider range of redshifts  $z \sim 0.02 - 0.63$ . The SFRs of LCGs are high at  $\sim 0.7 - 60 M_\odot \text{yr}^{-1}$  and overlap with those of LBGs.

Izotov et al. (2011, see also Guseva et al. (2009) and Zhao et al. (2010)) showed that LBGs, LCGs, luminous metal-poor star-forming galaxies (Hoyos et al. 2005), extremely metal-poor emission-line galaxies at  $z < 1$  (Kakazu et al. 2007), and low-redshift blue compact dwarf (BCD) galaxies with strong star-formation activity obey a common luminosity-metallicity relation. Finally, Izotov et al. (2014a) considered luminosity-metallicity and mass-metallicity relations for SDSS DR7 star-forming galaxies, which are much flatter than the Tremonti et al. (2004) relations. They also found that low- $z$  galaxies with high SFRs do not deviate from the relation established for galaxies with lower SFRs.

The above discussion implies some inconsistency between results obtained in different papers and raises the question: are luminosity- and mass-metallicity relations between global parameters of low- $z$  and high- $z$  star-forming galaxies different? What is the impact of different selection criteria and methods used for the determination of the galaxy metallicities? In this paper we attempt to study similarities and differences of the relations for star-forming galaxies in a redshift range  $0 < z < 3$ . Special care has been taken to use strong-line methods to derive the metallicity, which were calibrated using the  $T_e$ -method, based on the electron temperature determination from the  $[\text{O III}](\lambda 4959 + \lambda 5007)/\lambda 4363$  flux ratio (e.g. Izotov et al. 2011), and thus give consistent gas-phase metallicities. We also selected only compact star-forming galaxies with high-excitation H II regions, for which both methods can be applied. Furthermore, excitation conditions in those H II regions are similar to those in high- $z$  galaxies.

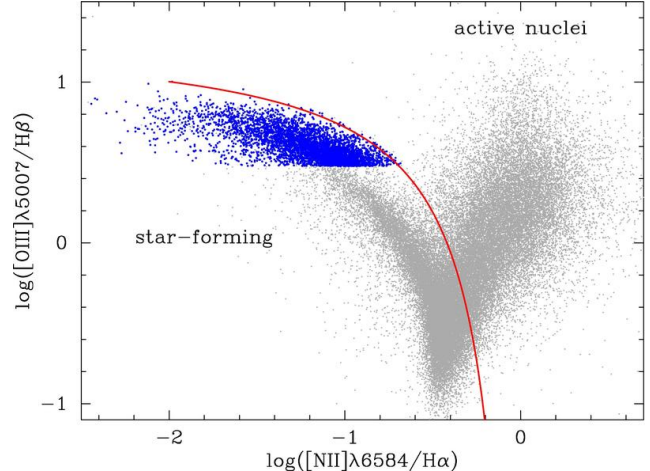


**Figure 1.** The Baldwin-Phillips-Terlevich (BPT) diagnostic diagram (Baldwin et al. 1981). Selected SDSS compact star-forming galaxies with  $[\text{O III}]\lambda 4959/H\beta \geq 1.0$ , corresponding to  $\log [\text{O III}]\lambda 5007/H\beta \gtrsim 0.5$ , and detected  $[\text{N II}]\lambda 6584$  line are shown by blue filled circles. Also plotted are all emission-line galaxies from SDSS DR7 (cloud of grey dots). The red solid line from Kauffmann et al. (2003) separates star-forming galaxies from active galactic nuclei.

In Sect. 2 we discuss the sample. The technique used for the determination of luminosities and stellar masses is described in Sect. 3. Different methods of the oxygen abundance determination are discussed in Sect. 4. Relations between different global parameters for our SDSS sample and comparisons with respective relations for high- $z$  galaxies with high-excitation H II regions are presented in Sect. 5. The main results of the paper are described in Sect. 6.

## 2 THE SAMPLE

The sample of compact star-forming galaxies was selected from the spectroscopic data base of the SDSS DR7 (Abazajian et al. 2009) and SDSS/BOSS DR10 (Ahn et al. 2014; Dawson et al. 2013; Smee et al. 2013). The criteria were: 1) only galaxies with angular diameters  $\lesssim 6''$  were selected to minimize the aperture corrections of the derived luminosities and stellar masses. As a measure of the angular size we used the Petrosian radius  $R_{50}$  with a 50% flux of the galaxy inside it in the SDSS  $r$  band. These data are available in the SDSS data base. The oxygen abundance is then characterizing the entire galaxy because of its compactness; 2) spiral galaxies are excluded. The oxygen abundances in individual H II regions are not representative characteristics for an entire spiral galaxy because of the abundance gradients in those galaxies; 3) galaxies with emission-line ratios  $[\text{O III}]\lambda 4959/H\beta < 1.0$  were excluded to ensure that only galaxies with high-excitation H II regions are included, for which the determination of extinction and chemical composition is more reliable. We note that most of high-redshift emission-line galaxies satisfy the criterion  $[\text{O III}]\lambda 4959/H\beta \geq 1.0$ , and hence have similar excitation conditions in their H II regions; 4) galaxies with AGN activity are excluded. We used obvious AGN spectral characteristics: broad emission lines (QSOs and Sy1 galaxies), the presence of strong high-ionisation  $[\text{Ne V}] \lambda 3426$  and He II

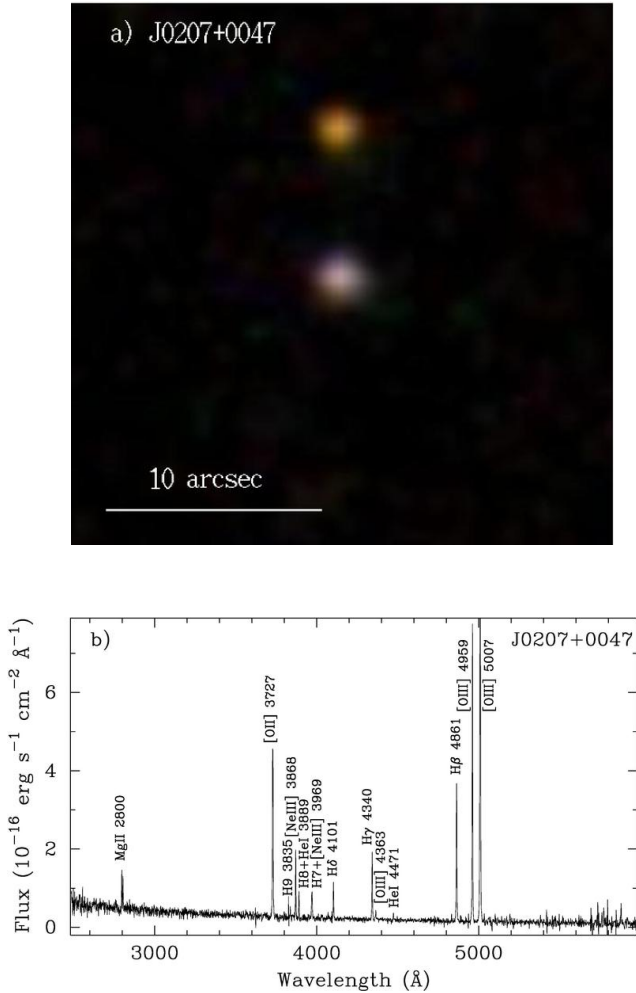


**Figure 2.** (a) The  $25'' \times 25''$  SDSS image centered on the compact star-forming galaxy J0207+0047. (b) The rest-frame SDSS spectrum of J0207+0047. The galaxy is located at a redshift of  $z = 0.54$ .

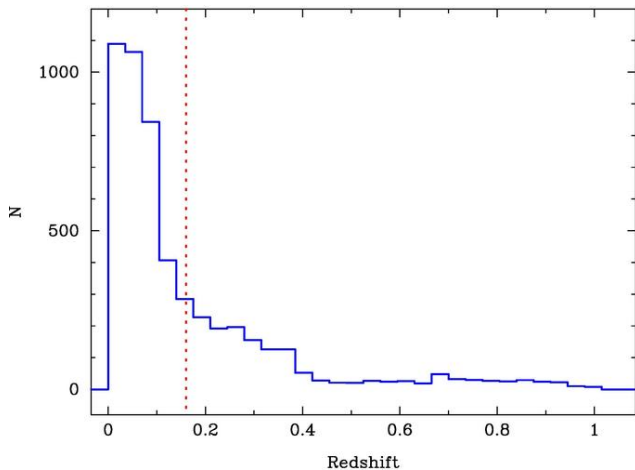


**Figure 3.** Distribution over redshift  $z$  of the SDSS compact star-forming galaxies from the entire sample. The dotted vertical line indicates the average redshift of 0.16.

$\lambda 4686$  emission lines in high-excitation spectra of Sy2 galaxies. Strong high-ionisation nebular [O III] emission lines are simultaneously observed with strong low-ionisation nebular [O I], [O II], [N II], and [S II] emission lines in many high-excitation Sy2 spectra. LINERs are excluded by a condition  $[\text{O III}]\lambda 4959/\text{H}\beta < 1.0$ . The reliability of our selection is checked with the diagnostic diagram, proposed by Baldwin et al. (1981) (BPT diagram, Fig. 1). All galaxies from our sample are located in the region of star-forming galaxies (blue dots in Fig. 1).

Applying these criteria, we selected 5182 galaxies in the redshift range  $0 < z < 1$ . The [O III]  $\lambda 4363$  emission line was detected at a level higher than  $1\sigma$  in 3607 galaxies from our sample, allowing us to obtain oxygen abundances by the  $T_e$ -method. Hereafter this subsample will be called “ $T_e$  sample”. We apply strong-emission-line (SEL) methods to derive oxygen abundances for the remaining subsample of 1575 galaxies.

The SDSS image of one compact galaxy from our sample, J0207+0047, is shown in Fig. 2a. This galaxy is located at the redshift  $z = 0.54$  and is very compact and is almost unresolved. Its angular diameter is only  $2R_{50} = 1.4''$ , corresponding to a linear diameter of  $\sim 30$  kpc. However, since this galaxy is unresolved, its true linear diameter can be much smaller. This is a common property for distant galaxies from our sample with  $z \gtrsim 0.2 - 0.3$ . *HST* images of a few compact star-forming galaxies at  $z \sim 0.1 - 0.35$  reveal that all of them have linear diameters less than 3 kpc (Cardamone et al. 2009; Jaskot & Oey 2014, Izotov et al. 2015, in preparation). The spectrum of J0207+0047 (Fig. 2b) is characterised by strong narrow emission lines and blue continuum. Spectra of all our galaxies have similar characteristics. They are very different from the spectra of “normal” galaxies dominated by numerous absorption lines and much redder continua. The spectrum in Fig. 2b is also very different from typical spectra of star-forming galaxies with weak emission lines, which were selected by Tremonti et al. (2004).

The redshift distribution of our entire sample with the average redshift of 0.16 (dotted vertical line) is shown in Fig. 3.

Spectroscopic data were supplemented with photometric data in five SDSS bands  $u$ ,  $g$ ,  $r$ ,  $i$ , and  $z$  for the entire galaxy and within the spectroscopic aperture, allowing aperture corrections of the observed fluxes and the determination of absolute galaxy magnitudes.

### 3 THE DETERMINATION OF GALAXY GLOBAL PARAMETERS

#### 3.1 Parameters of emission lines and dust extinction

We measured emission-line fluxes and equivalent widths using the IRAF<sup>1</sup> SPLIT routine. The line-flux errors include statistical errors in addition to errors introduced by

<sup>1</sup> IRAF is the Image Reduction and Analysis Facility distributed by the National Optical Astronomy Observatory, which is operated by the Association of Universities for Research in Astronomy (AURA) under cooperative agreement with the National Science Foundation (NSF).

the standard-star absolute flux calibration, which we set to 1% of the line fluxes. These errors will be later propagated into the calculation of abundance errors. Using the observed decrement of several hydrogen Balmer emission lines we corrected the line fluxes relative to the  $H\beta$  flux for two effects: (1) reddening adopting the extinction curve of Cardelli et al. (1989) and (2) underlying hydrogen stellar absorption that is derived simultaneously by an iterative procedure as described in Izotov et al. (1994). The extinction coefficients are defined as  $C(H\beta) = 1.47E(B-V)$ , where  $E(B-V) = A(V)/3.2$  (Aller 1984).

The spectroscopic data were corrected for the aperture using the relation  $2.5^{r(\text{app})-r}$ , where  $r$  and  $r(\text{app})$  are the SDSS  $r$ -band total magnitude and the magnitude within the round spectroscopic aperture, respectively. The diameters of spectroscopic apertures are  $3''$  and  $2''$  for the SDSS DR7 and SDSS/BOSS spectra, respectively. Selected galaxies are compact. Therefore the aperture corrections of fluxes are small, rarely exceeding the value of 2.

### 3.2 The absolute $g$ -band magnitudes and $H\beta$ luminosities

The extinction-corrected absolute  $g$ -band magnitudes  $M_g$  and extinction- and aperture-corrected  $H\beta$  luminosities  $L(H\beta)$  were obtained respectively from the SDSS extinction-corrected  $g$  magnitude for the entire galaxy and extinction- and aperture-corrected  $H\beta$  emission-line flux. The distance is derived from the redshift. For distance determination we used the relation  $D = f(z, H_0, \Omega_M, \Omega_\Lambda)$  from Refsdal et al. (1967), where the Hubble constant  $H_0 = 67.3 \text{ km s}^{-1} \text{ Mpc}^{-1}$  and cosmological parameters,  $\Omega_M = 0.273$  and  $\Omega_\Lambda = 0.682$ , were obtained from the *Planck* mission data (Ade et al. 2014). The equivalent widths  $\text{EW}(H\beta)$  were correspondingly reduced to the rest frame.

### 3.3 Spectral energy distribution (SED) and the galaxy's stellar masses

The stellar mass is one of the most important global galaxy characteristics. For its determination we follow the prescriptions described by Guseva et al. (2006, 2007) and Izotov et al. (2011, 2014a,b).

The method is based on fitting a series of model SEDs to the observed one and finding the best fit. It consists of the following. The fit was performed for each SDSS spectrum over the entire observed spectral range of  $\lambda\lambda 3900\text{--}9200\text{\AA}$  for SDSS DR7 galaxies and of  $\lambda\lambda 3600\text{--}10300\text{\AA}$  for SDSS/BOSS galaxies. As each SED is the sum of both stellar and ionised gas emission, its shape depends on the relative contribution of these two components. In galaxies with high  $\text{EW}(H\beta) > 50\text{\AA}$ , the ionised gas continuum is strong and is subtracted before fitting the stellar SED. Izotov et al. (2011) noted the importance of gaseous continuum subtraction, otherwise stellar masses of galaxies with high  $\text{EW}(H\beta)$ 's in their spectra would be overestimated by a factor of  $\sim 3$  or more. Hence, for the spectra of galaxies with  $\text{EW}(H\beta) > 50\text{\AA}$ , SED fitting and subtraction of the ionised gas emission in the continuum and emission lines are mandatory. Photometric data are not sufficient in these cases.

We carried out a series of Monte Carlo simulations to

reproduce the SED of each galaxy in our sample. To derive the stellar SED, we use a grid of instantaneous burst SEDs in a wide range of ages from 0.5 Myr to 15 Gyr calculated with package PEGASE.2 (Fioc & Rocca-Volmerange 1997). We adopted a stellar initial mass function with a Salpeter slope, an upper mass limit of  $100 M_\odot$ , and a lower mass limit of  $0.1 M_\odot$ . Then the SED with any star-formation history can be obtained by integrating the instantaneous burst SEDs over time with a specified time-varying star-formation rate.

The SED of the gaseous continuum was taken from Aller (1984). It included hydrogen and helium free-bound, free-free, and two-photon emission.

The star-formation history in each galaxy is approximated assuming a recent short burst with age  $t_y < 10$  Myr, which accounts for the young stellar population, and a prior continuous star formation for the older stars during the time interval between  $t_i$  and  $t_f$  ( $t_f < t_i$  and zero age is now). The contribution of each stellar population to the SED was parameterized by the ratio  $b = M_y/M_o$ , where  $M_y$  and  $M_o$  are respectively the masses of the young and old stellar populations. Then the total stellar mass is  $M_* = M_y + M_o$ .

For each galaxy, we calculated  $10^4$  Monte Carlo models by randomly varying  $t_y$ ,  $t_i$ ,  $t_f$ , and  $b$ . The best modelled SED was found from  $\chi^2$  minimization of the deviation between the modelled and the observed continuum in five wavelength ranges, which are free of the emission lines and residuals of the night-sky lines. Typical stellar mass uncertainties for our sample galaxies are of  $\sim 0.1 - 0.2$  dex.

## 4 OXYGEN ABUNDANCES

One of the most reliable methods of the oxygen abundance determination is a  $T_e$ -method, which is based on the electron temperature derived from the  $([\text{O III}]\lambda 4959 + \lambda 5007)/\lambda 4363$  flux ratio. This method provides a good measure of the metallicity below about  $12 + \log \text{O}/\text{H} \lesssim 8.3$  (e.g. Pilyugin 2001; Pettini & Pagel 2004; Stasińska 2005). However, at super-solar metallicities the  $T_e$ -method tends to underestimate significantly the true metallicity (Stasińska 2005).

We apply the  $T_e$ -method for the  $T_e$  sample of the galaxies with  $[\text{O III}]\lambda 4363$  emission-line intensity measured at the level better than  $1\sigma$ . As it can be seen below, all these galaxies satisfy condition  $12 + \log \text{O}/\text{H} \lesssim 8.3$ . To determine oxygen abundances, we generally followed the procedures of Izotov et al. (1994, 1997, 2006), which are discussed in detail by e.g. Izotov et al. (2011, 2014a,b).

Recently, Palay et al. (2012) obtained new effective collision strengths for the  $[\text{O III}]$  transitions, which in the temperature range 10000 - 20000K are higher by  $\sim 20\%$  for the transitions  $[\text{O III}]\lambda 4959$ ,  $\lambda 5007$ , but are higher by only a few percent for the transition  $[\text{O III}]\lambda 4363$ . These updates in the atomic data would result in lower electron temperatures by  $\sim 500 - 700\text{K}$  and hence in higher oxygen abundances (Nicholls et al. 2013) as compared to those obtained with the Izotov et al. (2006) iterative procedure. However, this effect will increase  $12 + \log \text{O}/\text{H}$  by not more than  $\sim 0.05$  dex.

Nicholls et al. (2013) and Dopita et al. (2013) considered the possibility that electrons in  $\text{H II}$  regions may not be in thermal equilibrium, i.e. their velocity distribution deviates from a Maxwellian distribution. The overall effect will

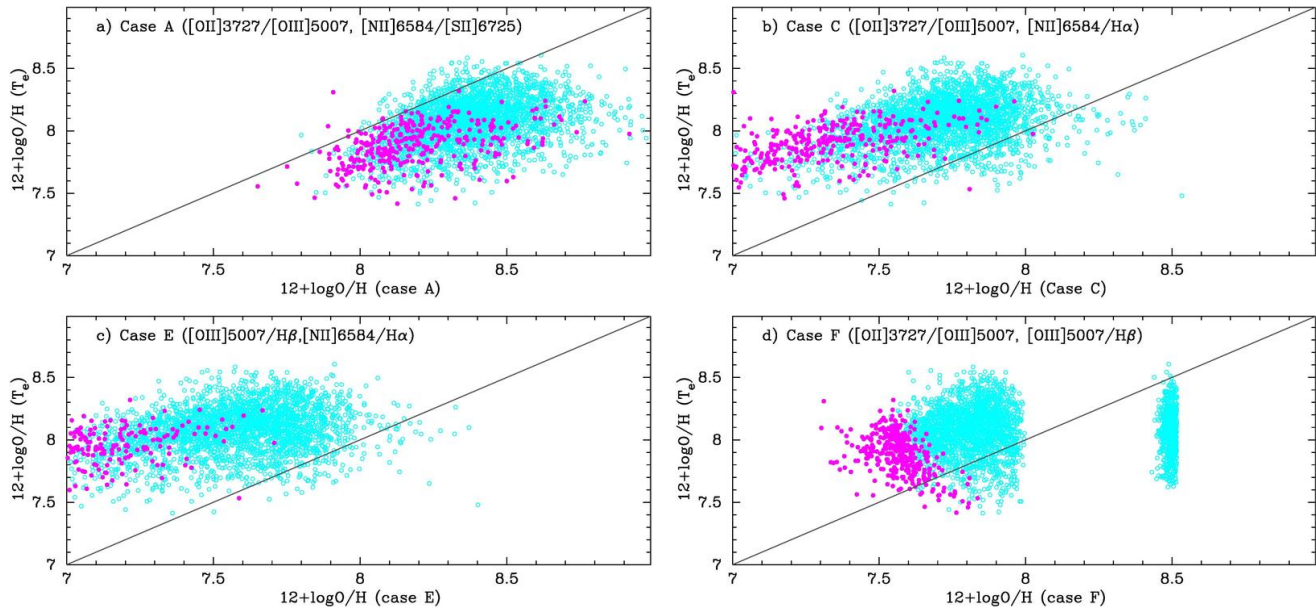


**Figure 4.** A comparison of oxygen abundances  $12 + \log O/H$ , derived by the  $T_e$ -method (this paper) and different strong-line methods from Charlot & Longhetti (2001) for our  $T_e$  sample. In each panel, the emission-line ratios used by strong-line methods are given in parentheses. Galaxies with  $O_{32} = [O \text{ III}]\lambda 5007/[O \text{ II}]\lambda 3727 \geq 4.5$  and  $< 4.5$  are given by magenta filled circles and cyan open circles, respectively. Solid lines show the one-to-one relations.

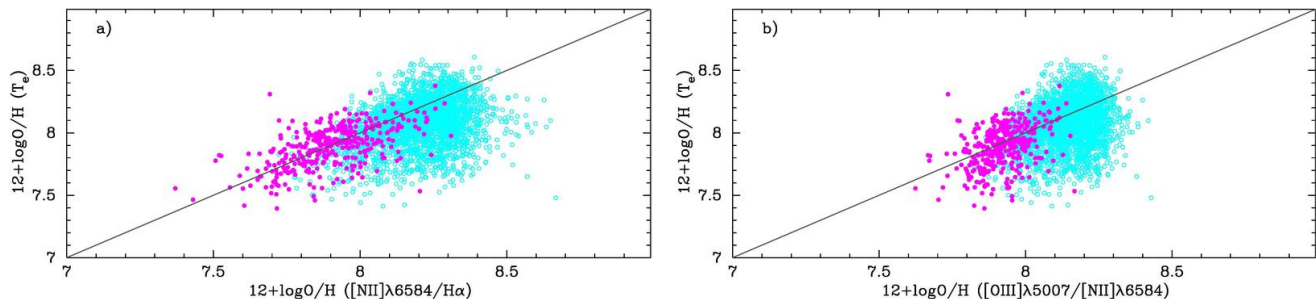


**Figure 5.** A comparison of oxygen abundances  $12 + \log O/H$  derived by the  $T_e$ -method (this paper) and strong-emission-line (SEL) methods proposed by Pettini & Pagel (2004), which utilize the (a)  $[N \text{ II}]\lambda 6584/H\alpha$  and (b)  $[O \text{ III}]\lambda 5007/[N \text{ II}]\lambda 6584$  line-intensity ratios. Shown are the same galaxies by the same symbols as in Fig. 4. Solid lines denote the one-to-one correlations.

be an increase of the oxygen abundance. However, for low-metallicity high-excitation H II regions selected in this study the increase of  $12 + \log O/H$  is unlikely to be higher than 0.2 dex (Dopita et al. 2013). We note that a deviation from the Maxwellian distribution is found in the solar wind, but not in H II regions. Therefore, we use equations by Izotov et al. (2006), which assume a Maxwellian distribution of electrons.

The SDSS spectra of most star-forming galaxies are noisy. Then the  $[O \text{ III}]\lambda 4363$  line is not detected or is measured with insufficient accuracy. In these cases, strong-line methods are commonly used to derive oxygen abundances instead of the  $T_e$ -method. There are two different approaches to obtain calibrations for the metallicity by using strong-line intensities. One approach is based on deriving the line intensities by producing a grid of H II region models with varying metallicity, ionisation parameter, and other input parameters (e.g. Charlot & Longhetti 2001; Kewley & Dopita 2002; Kobulnicky & Kewley 2004; Dawson et al. 2013). The second approach uses the empirical relations between certain combinations of strong-line intensities and metallicity, which

is derived by the  $T_e$ -method (e.g. Alloin et al. 1979; Pagel et al. 1979; Pilyugin 2001; Pettini & Pagel 2004; Pilyugin & Thuan 2005; Stasińska 2006; Pilyugin et al. 2010).

The advantage of all these SEL methods is that they are based on the strongest emission lines and thus can be applied to large galaxy samples. The disadvantage is that most of these methods depend not only on the metallicity, but also on the ionisation parameter. The detailed comparison of strong-line methods (e.g. Kewley & Dopita 2002; Kewley & Ellison 2008; Maiolino et al. 2008) shows that they are not consistent, non-monotonic (e.g. the  $R_{23}$ -method, Pagel et al. 1979; Kewley & Dopita 2002), depend on parameters different from metallicity and result in oxygen abundances, which can deviate by  $\sim 0.5$  dex or more.

To illustrate the problem we compare the oxygen abundances derived for the  $T_e$  sample by the  $T_e$ -method and different strong-line calibrations by Charlot & Longhetti (2001), which are based on population-synthesis and H II region models. Calibrations by Charlot & Longhetti (2001) were used by Tremonti et al. (2004) to produce luminosity-

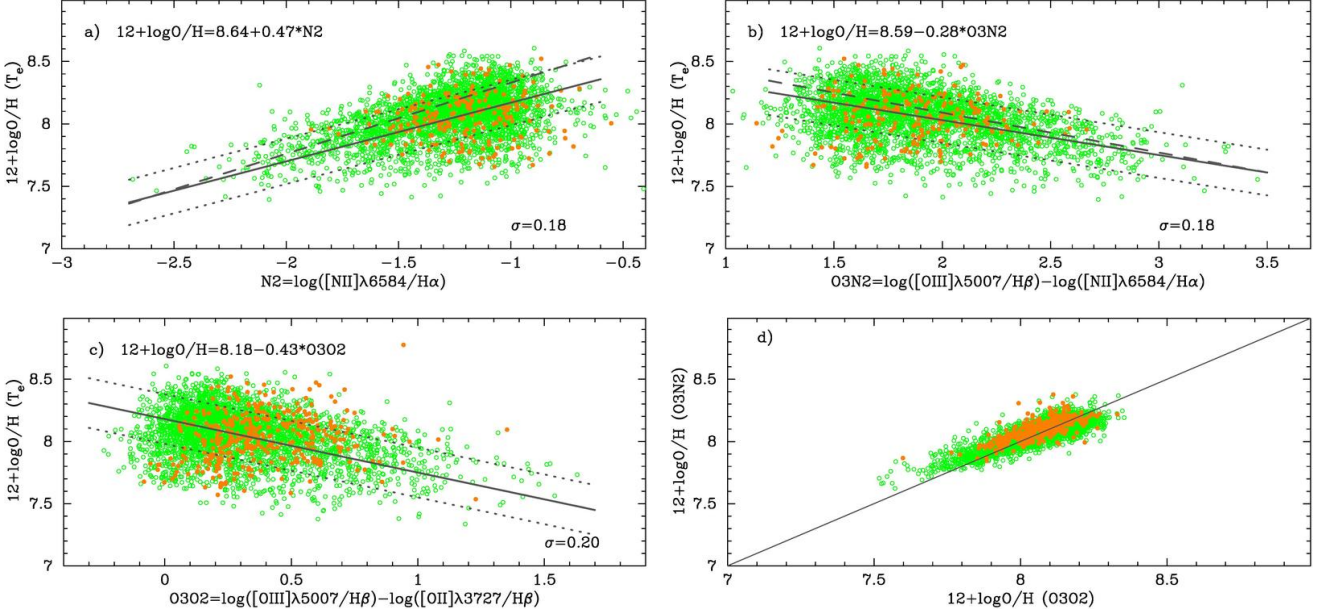


**Figure 6.** (a) - (c) Relations between the oxygen abundances  $12+\log\text{O}/\text{H}$  derived by the  $T_e$ -method and the line intensity ratios  $[\text{N II}]\lambda 6584/\text{H}\alpha$ ,  $[\text{O III}]\lambda 5007/[\text{N II}]\lambda 6584$ , and  $[\text{O III}]\lambda 5007/[\text{O II}]\lambda 3727$ , respectively. Shown are only the galaxies from the  $T_e$  sample. Solid and dotted lines represent maximum-likelihood fits to the data and  $1\sigma$  dispersions, respectively, dashed lines in (a) and (b) refer to the relations obtained by Pettini & Pagel (2004). (d) The relation between the oxygen abundances derived using the  $O3N2$  (Eq. 2) and  $O3O2$  (Eq. 3) calibrations. The solid line is the one-to-one correlation. Green open circles and brown filled circles in all panels correspond to galaxies with the redshifts  $z \leq 0.3$  and  $z > 0.3$ , respectively.

metallicity and mass-metallicity relations for a large sample of nearby SDSS star-forming galaxies. The Tremonti et al. (2004) relations are often used as templates of the present-day luminosity-metallicity and mass-metallicity relations for comparison with similar relations at higher redshifts.

We compare in Fig. 4 oxygen abundances derived by using the  $T_e$ -method and four out of seven strong-line calibrations by Charlot & Longhetti (2001), which are based on different emission-line intensities and their ratios. The sample is split into two parts with the extinction-corrected ratio  $O_{32} = [\text{O III}]\lambda 5007/[\text{O II}]\lambda 3727 \geq 4.5$  (small magenta filled circles) and  $< 4.5$  (small cyan open circles). The parameter  $O_{32}$  is an increasing function of the ionisation parameter at given metallicity. Among the Charlot & Longhetti (2001) calibrations the largest number of emission lines ( $[\text{O II}]\lambda 3727$ ,  $[\text{O III}]\lambda 5007$ ,  $[\text{N II}]\lambda 6584$  and  $[\text{S II}]\lambda 6717$ , 6731) is used in the calibration, which Charlot & Longhetti (2001) labelled as case A. We do not consider two calibrations by Charlot & Longhetti (2001), which use the blend of  $\text{H}\alpha$  and  $[\text{N II}]\lambda 6584$  emission lines. This is because the spectral resolution of the SDSS spectra is sufficient to separate these two lines. We also excluded from the consideration one calibration, which is based on the discontinuity parameter  $D_{4000}$  at  $\lambda \sim 4000\text{\AA}$ . This calibration is suitable for galaxies with absorption lines in their spectra.

It is seen in Fig. 4a that the oxygen abundance at low metallicities ( $12+\log\text{O}/\text{H} (T_e) \lesssim 8.1$ ) derived by the strong-line method (case A) is by  $\sim 0.2 - 0.3$  dex higher than that derived by the  $T_e$ -method. At higher metallicities the oxygen abundances derived by the two methods are very different. The comparison of the  $T_e$ -method with other strong-line

methods by Charlot & Longhetti (2001) (Fig. 4b – 4d) also indicates large inconsistencies.

Therefore, we conclude that the oxygen abundances, and consequently, the luminosity-metallicity and mass-metallicity relations for nearby SDSS star-forming galaxies, obtained by Tremonti et al. (2004), may not be correct, because they use a set of Charlot & Longhetti (2001) internally inconsistent calibrations.

A more promising way is to use empirical relations between line intensities and oxygen abundances derived by the  $T_e$ -method in real star-forming galaxies (e.g. Pettini & Pagel 2004). These relations can be obtained only for galaxies with high-excitation H II regions, where the  $[\text{O III}]\lambda 4363$  emission line can be detected. In Fig. 5 we compare oxygen abundances obtained by the  $T_e$ -method with those, which were obtained by using strong-line calibrations by Pettini & Pagel (2004). It is seen that abundances derived by different methods are in agreement despite the larger dispersion and small offset of  $\sim 0.1$  at  $12+\log\text{O}/\text{H} \geq 8.0$ .

Using only SDSS data for the large  $T_e$  sample we modified the Pettini & Pagel (2004) calibrations (Fig. 6) and obtained the maximum-likelihood linear relations

$$12 + \log \frac{\text{O}}{\text{H}} = 8.64 \pm 0.02 + (0.47 \pm 0.02) \times N2, \quad (1)$$

$$12 + \log \frac{\text{O}}{\text{H}} = 8.59 \pm 0.02 - (0.28 \pm 0.01) \times O3N2, \quad (2)$$

where  $N2 = \log([\text{N II}]\lambda 6584 / \text{H}\alpha)$ ,  $O3N2 = \log([\text{O III}]\lambda 5007 / \text{H}\beta) - \log([\text{N II}]\lambda 6584 / \text{H}\alpha)$ .

It is seen in Fig. 6 that relations by Pettini & Pagel (2004) (dashed lines) obtained for a smaller sample of H II regions, but for a larger range of oxygen abundances with

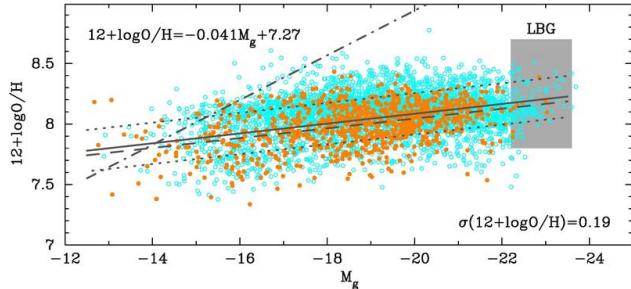


**Figure 7.** The relations between extinction-corrected absolute SDSS  $g$ -band magnitude  $M_g$  and oxygen abundance  $12+\log\text{O}/\text{H}$ . The galaxies with the  $[\text{O III}]\lambda 4363$  emission-line detection at a level higher than  $4\sigma$  shown by brown filled circles and the rest of the sample by cyan open circles. The solid line provides a linear maximum-likelihood fit to the data and dotted lines show  $1\sigma$  dispersions. The dashed line is a linear maximum-likelihood fit to the data shown by brown symbols. The steep dash-dotted line indicates the relation by Tremonti et al. (2004). The location of Lyman-break galaxies (LBGs) at  $z \sim 3$  by Pettini et al. (2001) is marked by a grey rectangle.

inclusion of high-metallicity H II regions, are not very different from the relations Eqs. 1 and 2 (solid lines) obtained in this paper. However, the difference is smaller ( $\leq 0.1$  for  $12 + \log\text{O}/\text{H}$ ) in the case of  $O3N2$  calibrations (Fig. 6b). The galaxies from our entire sample were selected using the same selection criteria, as the  $T_e$  sample, i.e. H II regions in these galaxies are of high excitation. The only difference is that the  $[\text{O III}]\lambda 4363$  was measured with insufficient accuracy or not detected in many galaxies. Therefore, calibrations Eqs. 1 and 2 can be applied for the entire sample.

However, there are 638 galaxies from the entire sample, including 264 galaxies from the  $T_e$  sample, where the  $[\text{N II}]\lambda 6584$  emission line has not been measured because of its weakness or because this line is outside the SDSS wavelength range in high-redshift galaxies with  $z \gtrsim 0.40$  of the SDSS DR7 survey and  $z \gtrsim 0.55$  of the SDSS/BOSS survey. In all these cases, with exception of the galaxies from the  $T_e$  sample, we use the relation between the oxygen abundance  $12+\log\text{O}/\text{H}$  and the parameter  $O3O2 = \log([\text{O III}]\lambda 5007/[\text{O II}]\lambda 3727)$  derived for the  $T_e$  sample (Fig. 6c)

$$12 + \log \frac{\text{O}}{\text{H}} = 8.18 \pm 0.01 - (0.43 \pm 0.02) \times O3O2. \quad (3)$$

We compare in Fig. 6d oxygen abundances derived from Eqs. 2 and 3. It is seen that  $12 + \log\text{O}/\text{H}$  obtained with the both  $O3N2$  and  $O3O2$  calibrations are nearly identical. Furthermore, in all panels of Fig. 6 there is no evident offset between the galaxies with low redshifts  $z \leq 0.3$  (green open circles) and higher redshifts  $z > 0.3$  (brown filled circles), implying that all three relations Eqs. 1 – 3 can be applied in the entire range of redshifts.

Summarising, we derive oxygen abundances (1) by the  $T_e$ -method in 3607 galaxies, (2) by using Eq. 3 in 638 – 264 = 374 galaxies, and (3) by using Eq. 2 in the remaining galaxies.

## 5 RESULTS

### 5.1 Absolute $g$ -band magnitude - metallicity relation

The extinction-corrected absolute  $g$ -band magnitude - metallicity relation for the entire sample of star-forming galaxies is shown in Fig. 7. The maximum-likelihood linear regression,

$$12 + \log \frac{\text{O}}{\text{H}} = -(0.041 \pm 0.002)M_g + 7.27 \pm 0.03, \quad (4)$$

is shown by a solid line and  $1\sigma$  deviations by dotted lines. For comparison, we show by dashed line the maximum-likelihood linear regression for the  $T_e$  subsample with the  $[\text{O III}]\lambda 4363$  emission line detected at the level higher than  $4\sigma$ . The difference between these two relations is very small, less than 0.05 in  $12 + \log\text{O}/\text{H}$ . This indicates that decreasing the detection limit for the  $[\text{O III}]\lambda 4363$  emission line to  $1\sigma$  and including galaxies with  $12 + \log\text{O}/\text{H}$  derived by  $O3N2$  or  $O3O2$  calibrations leads to a higher dispersion by a factor of  $\sim 2$  but does not introduce significant offsets in  $12 + \log\text{O}/\text{H}$ .

The relation in Eq. 4 is slightly flatter than that obtained by Guseva et al. (2009) and Izotov et al. (2011). However, we note that Guseva et al. (2009) and Izotov et al. (2011) considered not only SDSS galaxies but also galaxies from other samples with a large fraction of low-metallicity galaxies. Our sample is more uniform and includes only SDSS compact galaxies. The  $M_g - 12+\log\text{O}/\text{H}$  relation for this sample is very similar to that derived by Izotov et al. (2014a) for a much smaller sample of SDSS compact star-forming galaxies.

Our  $g$ -band absolute magnitude - metallicity relation is much flatter than that obtained by Tremonti et al. (2004) for a sample of  $\sim 53000$  star-forming galaxies selected from the SDSS (dash-dotted line in Fig. 7). This difference arises primarily because of different methods applied for the metallicity determination and because of the selection criteria used in both studies. Our sample consists of compact galaxies with high-excitation H II regions, and we applied strong-line methods, which give oxygen abundances consistent with the  $T_e$ -method, at variance with Charlot & Longhetti (2001) calibrations used by Tremonti et al. (2004). Furthermore, most of the star-forming galaxies from the Tremonti et al. (2004) sample are galaxies with low-excitation H II regions, for which the determination of metallicities is more uncertain compared to galaxies with high-excitation H II regions. Since empirical calibrations inferred from observations are not available for low-excitation H II regions because of the very weak and undetectable  $[\text{O III}]\lambda 4363$  emission lines, we do not consider these galaxies.

On the other hand, the location of star-forming galaxies at  $0 < z < 1$  with high luminosities is similar to that for the Ly-break galaxies (LBGs) by Pettini et al. (2001), shown by a box in Fig. 7. This is consistent with a universal character of the  $M_g - 12+\log\text{O}/\text{H}$  relation for star-forming galaxies with high-excitation H II regions in the entire redshift range  $0 < z < 3$ .

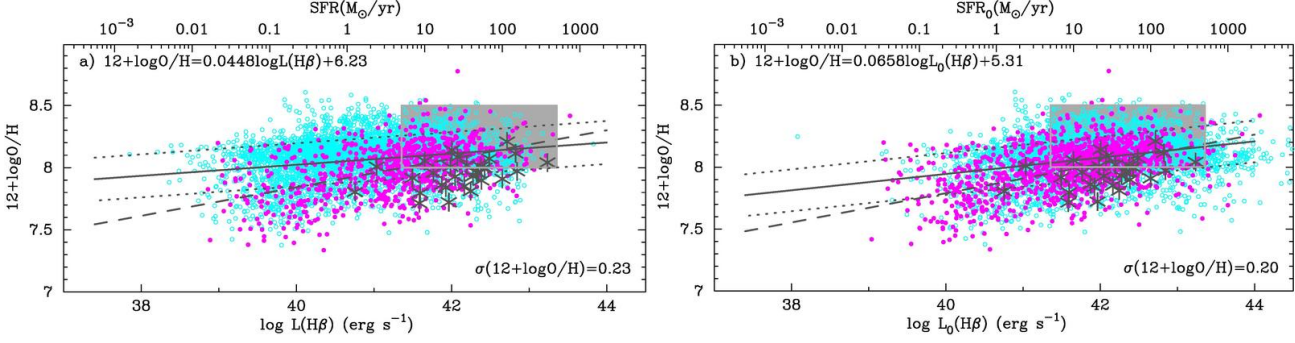


**Figure 8.** The  $H\beta$  luminosity-metallicity relation. The upper axis indicates the scale of the star-formation rate, calculated with Kennicutt (1998) calibration. Galaxies with the equivalent widths  $EW(H\beta) < 100\text{\AA}$  and  $\geq 100\text{\AA}$  are shown by the open cyan circles and filled magenta circles, respectively. The  $H\beta$  luminosities in panel (a) are corrected for extinction and aperture, while they are additionally reduced to zero starburst age in panel (b). Solid lines in both panels are maximum-likelihood linear fits to all data and dotted lines are  $1\sigma$  dispersions. The dashed lines are maximum-likelihood linear fits only for the galaxies with  $EW(H\beta) \geq 100\text{\AA}$  shown by magenta symbols. The location of star-forming galaxies with redshifts  $2.0 < z < 2.6$  by Steidel et al. (2014) and with redshifts  $z > 2$  by Cullen et al. (2014) is shown by grey rectangles. Star-forming galaxies with redshifts  $z \sim 3.4$  by Troncoso et al. (2014) are indicated by dark asterisks.

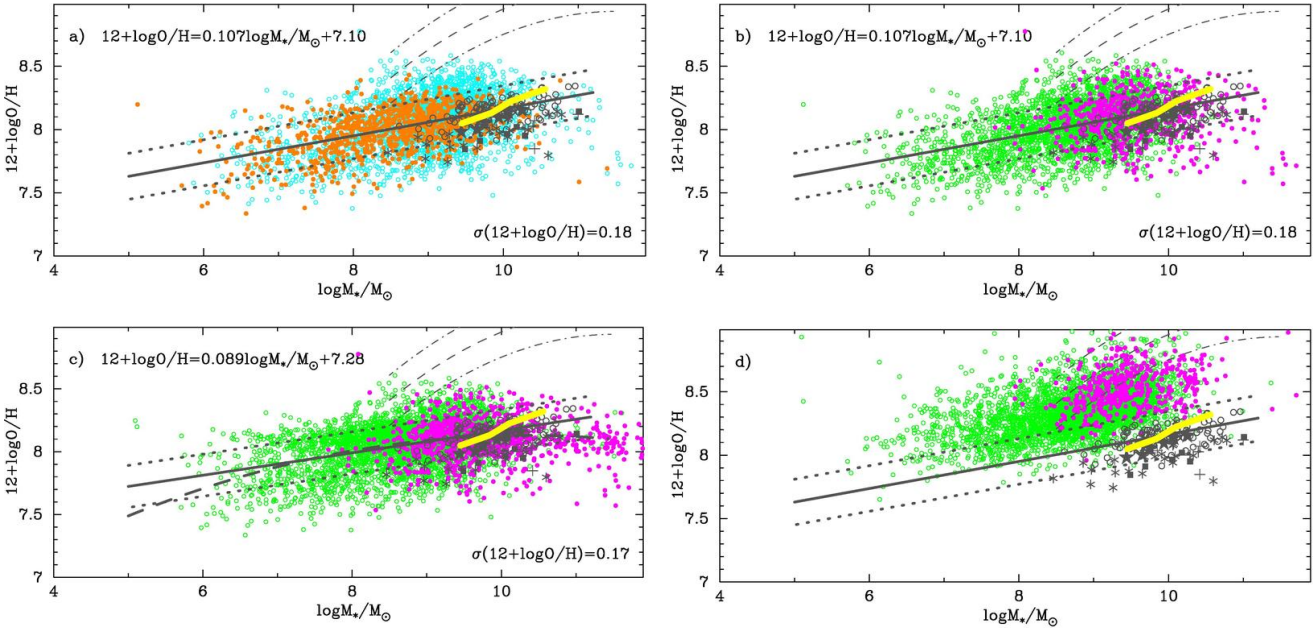


**Figure 9.** The stellar mass - metallicity relations for (a) – (b) the  $T_e$  and (c) – (d) the entire sample. Brown symbols in (a) correspond to the galaxies, where  $[O\ III]\lambda 4363$  emission is detected at a level better than  $4\sigma$ , while cyan symbols are for the rest of the galaxies. Galaxies shown with magenta and green symbols in (b) – (d) have  $SFR \geq 10 M_\odot \text{ yr}^{-1}$  and  $< 10 M_\odot \text{ yr}^{-1}$ , respectively. Thick solid lines in (a) – (c) represent maximum-likelihood linear fits to the data in respective panels and dotted lines indicate  $1\sigma$  dispersions. The thick dashed line in (c) is the maximum-likelihood quadratic fit to the data. The thick solid line in (d) is the maximum-likelihood linear fit to the data in (a). The relation by Tremonti et al. (2004) is shown by thin dashed lines and dot-dashed lines are  $1\sigma$  dispersions. The location of stacked data for star-forming galaxies at  $z > 2$  by Cullen et al. (2014) and of data for ninety six star-forming galaxies at  $2.0 < z < 2.6$  by Steidel et al. (2014) are shown by dark-grey filled stars and open circles, respectively. Star-forming galaxies at  $z \sim 3.5$  by Maiolino et al. (2008) and at  $z \sim 2$  by Maier et al. (2014) are shown by dark-grey filled squares and crosses, respectively. Thirty star-forming galaxies with redshifts  $z \sim 3.4$  by Troncoso et al. (2014) are indicated by asterisks. The relation for  $z \sim 2.3$  by Sanders et al. (2015) is shown by thick yellow solid line. Oxygen abundances for all high- $z$  galaxies are calculated with  $O3N2$  or  $O3O2$  calibrations from this paper (Eqs. 2 – 3). (d) Same as in (c), but oxygen abundances are derived using the Charlot & Longhetti (2001) strong-line method (case A).

## 5.2 $H\beta$ luminosity - metallicity relation

$H\beta$  emission is a signature of the youngest stellar population in star-forming galaxies and the  $H\beta$  luminosity allows us to estimate the SFR using, e.g., the relation by Kennicutt (1998) between SFR and  $H\alpha$  luminosity. However, we note that the use of the relation by Kennicutt (1998) is not well

justified for starburst galaxies because of uncertainties in the adopted duration of the burst. The  $H\beta$  and  $H\alpha$  luminosities are more reliable characteristics, because they are directly derived from observations.

The UV,  $H\beta$  and mid-infrared luminosities of compact star-forming galaxies are tightly correlated (e.g. Izotov et



al. 2014a) indicating that the radiation of young stellar populations is a dominant source of dust heating and of galaxy emission in the UV range and H $\beta$  line. Consequently, SFRs derived by different methods for star-forming galaxies in a wide range of redshifts can be compared.

In Fig. 8a we show the extinction- and aperture-corrected H $\beta$  luminosity – oxygen abundance relation for our entire sample. The upper axis denotes the SFR calculated with the Kennicutt (1998) relation. The box indicates the location of star-forming galaxies with redshifts  $2.0 < z < 2.6$  by Steidel et al. (2014) and with  $z > 2$  by Cullen et al. (2014). Star-forming galaxies with  $z \sim 3.4$  by Troncoso et al. (2014) are indicated by asterisks. Strong emission lines with  $[\text{O III}]\lambda 4959/\text{H}\beta \gtrsim 1$  are present in spectra of most galaxies from their samples. Therefore, strong-line methods calibrated with the  $T_e$ -method can be applied. Steidel et al. (2014) compared SFRs obtained for their sample from the UV continuum luminosities and H $\alpha$  luminosities and found good agreement. They derived oxygen abundances by using strong-line O3N2 calibration, similar to that applied for our sample. To derive metallicities Cullen et al. (2014) and Troncoso et al. (2014) used empirical calibrations by Maiolino et al. (2008), which also were calibrated with the use of galaxy samples, where oxygen abundances were derived by the  $T_e$ -method. However, for consistency reasons we selected only high- $z$  galaxies with  $[\text{O III}]\lambda 4959/\text{H}\beta \geq 1$  and recalculated their oxygen abundances using Eqs. 2 or 3.

Despite the noisy data for high- $z$  galaxies there is a good coincidence in Fig. 8a between the luminous tail in the distributions of our galaxies and the high- $z$  galaxies, indicating the universal character of the  $L(\text{H}\beta) - 12 + \log \text{O}/\text{H}$  relation for star-forming galaxies with high-excitation H II regions.

However, we note the offset between the distributions of the galaxies with  $\text{EW}(\text{H}\beta) \geq 100\text{\AA}$  (magenta symbols and dashed line) and of the galaxies with  $\text{EW}(\text{H}\beta) < 100\text{\AA}$  (cyan symbols and solid line). This difference is primarily due to the fact that starbursts with high  $\text{EW}(\text{H}\beta)$  are on average younger. The H $\beta$  emission is powered by the ionising radiation and its luminosity strongly declines with the age of starburst. According to the Starburst99 models (Leitherer et al. 1999) the number of ionising photons and, respectively, the H $\beta$  luminosity produced by a burst is constant during the first 3 Myr. After that time it declines and is lower by a factor of  $\sim 50$  at a starburst age of 10 Myr. On the other hand, the luminosity of non-ionising radiation at  $\sim 1500\text{\AA}$  during the same time interval is decreased only by a factor of  $\sim 2$ . Since galaxies are observed with different starburst ages, their H $\beta$  luminosities, for consistency, should be reduced to zero age. The H $\beta$  equivalent width can be used for this, because it depends on the starburst age. We use Starburst99 models to derive the correction of the H $\beta$  luminosity for the starburst age,

$$\Delta \log L(\text{H}\beta) = 2.553 - \log[\text{EW}(\text{H}\beta)] \quad (5)$$

for  $\log \text{EW}(\text{H}\beta) \leq 2.553$ , otherwise  $\Delta \log L(\text{H}\beta) = 0$ . The relation Eq. 5 is correct for instantaneous bursts and may overestimate the correction of the H $\beta$  luminosity for the starburst age if underlying older stellar population is present. Our SED fitting shows that the contribution of an older stellar population to the stellar continuum near the H $\beta$  emission line in galaxies with strong emission lines varies in a wide range of  $\sim 5\% - 50\%$ . This results in an overestimation of

$\log L(\text{H}\beta)$  by  $\lesssim 0.3$ . The effect is stronger for galaxies with low  $\text{EW}(\text{H}\beta)$ .

In Fig. 8b we show the relation between the H $\beta$  luminosity  $L_0(\text{H}\beta)$  reduced to zero age and the oxygen abundance. It is seen that the differences between maximum-likelihood linear fits for our two samples (solid and dashed lines) are reduced and distributions of data are in better agreement compared to Fig. 8a, implying that the age correction should be applied for consistent comparison of H $\beta$  and H $\alpha$  luminosities and star-formation rates in star-forming galaxies.

### 5.3 Stellar mass - metallicity relation

In Fig. 9a we show the extinction- and aperture-corrected stellar mass - metallicity relations for the  $T_e$  sample. The sample is split into two subsamples with  $[\text{O III}]\lambda 4363$  emission line detected at the level better than  $4\sigma$  (small filled brown circles) and in the range  $1\sigma - 4\sigma$  (small open cyan circles). The data for the  $T_e$  sample can be fitted by a linear relation, as shown in Fig. 9a by the solid line,

$$12 + \log \frac{\text{O}}{\text{H}} = (0.107 \pm 0.004) \log \frac{M_*}{M_\odot} + 7.10 \pm 0.04. \quad (6)$$

The dispersion for the subsample with weaker  $[\text{O III}]\lambda 4363$  lines is characterised by a factor of  $\sim 2$  higher value, but no offset relative to the subsample with stronger lines is present. Similarly, the subsample with high star-formation rate  $\text{SFR} \geq 10 M_\odot \text{ yr}^{-1}$  (small filled magenta circles in Fig. 9b) follows the same relation as the subsample with low  $\text{SFR} < 10 M_\odot \text{ yr}^{-1}$  (small open green circles), indicating that there is no obvious dependence of the metallicity on SFR.

In Fig. 9c the stellar mass – metallicity relation is shown for the entire sample. Adding the galaxies with the oxygen abundance derived with strong-line methods results in a flattening of the relation at  $M_* \geq 10^{10} M_\odot$ . Linear regression yields

$$12 + \log \frac{\text{O}}{\text{H}} = (0.089 \pm 0.004) \log \frac{M_*}{M_\odot} + 7.28 \pm 0.04. \quad (7)$$

However, better agreement can be obtained with the quadratic stellar mass – metallicity relation

$$12 + \log \frac{\text{O}}{\text{H}} = \log \frac{M_*}{M_\odot} \left( 0.023 \log \frac{M_*}{M_\odot} + 0.466 \right) + 5.72 \quad (8)$$

shown in Fig. 9c by a thick dashed line. These relations are similar to the relation obtained by Izotov et al. (2014a) for a smaller sample of SDSS galaxies.

On the other hand, the stellar mass-metallicity relations in Fig. 9a – 9c (solid lines) are much flatter and are shifted to lower metallicities compared to that obtained by Tremonti et al. (2004) (thin dashed lines). In part, this difference may be caused by different selection criteria. However, we argue that the main cause of the difference is the use of different methods for the oxygen abundance determination, as discussed above. We show in Fig. 9d the stellar mass – metallicity relation for the entire sample, same as in Fig. 9c, but with oxygen abundances derived by the Charlot & Longhetti (2001) calibration, which has been used by Tremonti et al. (2004). It is seen that agreement with the Tremonti et al. (2004) relation is much better if the Charlot & Longhetti

**Table 1.** Average oxygen abundances for the entire sample in the four stellar mass intervals

SFR ( $M_{\odot}\text{yr}^{-1}$ )	$12+\log\text{O}/\text{H}^{\text{a}}$			
	9.0 – 9.2 <sup>b</sup>	9.4 – 9.6 <sup>b</sup>	10.0 – 10.2 <sup>b</sup>	10.4 – 10.6 <sup>b</sup>
0.1 - 1	8.10±0.18 (205)	8.12±0.16 (142)	...	...
1 - 5	8.10±0.16 (147)	8.14±0.15 (163)	8.12±0.16 ( 25)	8.14±0.09 ( 6)
5 - 10	8.11±0.15 ( 67)	8.14±0.13 ( 69)	8.12±0.15 ( 24)	8.15±0.07 ( 4)
10 - 20	8.12±0.16 ( 52)	8.12±0.20 ( 42)	8.15±0.16 ( 30)	8.09±0.13 ( 5)
20 - 50	8.12±0.15 ( 27)	8.07±0.18 ( 46)	8.13±0.11 ( 28)	8.09±0.21 ( 15)
> 50	...	8.08±0.15 ( 22)	7.98±0.20 ( 14)	8.12±0.13 ( 9)

<sup>a</sup>The number of galaxies used for averaging is shown in parentheses.

<sup>b</sup> interval of  $\log M_{*}/M_{\odot}$ .

(2001) calibration is used. However, this calibration is not consistent with the  $T_{\text{e}}$ -method, as it was discussed above.

It was argued in some recent papers (e.g. Manucci et al. 2010; Lara-López et al. 2010; Hunt et al. 2012; Andrews & Martini 2013) that star-forming galaxies with higher SFRs are systematically more metal-poor on the stellar mass-metallicity diagrams. In particular, Manucci et al. (2010) proposed a fundamental metallicity relation (FMR) between stellar mass, gas-phase metallicity and star formation rate.

We checked whether the tendency of lower metallicity in galaxies with higher SFR is present for galaxies from our sample. To exclude the dependence of the oxygen abundance on the stellar mass we calculated average  $12 + \log\text{O}/\text{H}$  for galaxies from the entire sample in the four narrow ranges of stellar masses and for different ranges of SFR (Table 1). We find no evidence that the galaxies with high SFRs are systematically more metal-poor, confirming conclusions by Izotov et al. (2014a). We also applied the  $\chi^2$  minimization technique for samples shown in Fig. 9b in the plane [ $\mu_{\alpha} = \log(M_{*}/M_{\odot}) - \alpha\log\text{SFR}(M_{\odot}\text{yr}^{-1})$ ] – metallicity and find  $\alpha \sim 0$ , i.e. no dependence on SFR is detected.

Manucci et al. (2010) argued that introducing  $\mu_{\alpha}$  with  $\alpha = 0.32$  eliminates any redshift evolution up to  $z \sim 2.5$  yielding the same  $\mu_{\alpha}$  – metallicity relation independent of redshift (see also Sect. 1). To verify this conclusion with our sample we show in Fig. 9 star-forming galaxies at  $z > 2$  by Cullen et al. (2014) (stars), star-forming galaxies at  $2.0 < z < 2.6$  by Steidel et al. (2014) (filled circles), star-forming galaxies at redshifts  $z \sim 3.5$  by Maiolino et al. (2008) (filled squares), star-forming galaxies with  $z \sim 2$  by Maier et al. (2014) (crosses), and star-forming galaxies with  $z \sim 3.4$  by Troncoso et al. (2014) (asterisks). The relation for galaxies with  $z \sim 2.3$  by Sanders et al. (2015) is shown by thick yellow solid line. For homogeneity, only high- $z$  galaxies with  $[\text{O III}]\lambda 4959/\text{H}\beta \geq 1$  and oxygen abundances derived by Eqs. 2 or 3 are shown. It is seen that high- $z$  galaxies are closely related to lower- $z$  counterparts and do not indicate any appreciable dependence of the mass – metallicity relation on redshift. However, we note that the high- $z$  data by Maiolino et al. (2008), Troncoso et al. (2014), and Maier et al. (2014) are offset to lower metallicities compared to the data by Cullen et al. (2014) and Steidel et al. (2014). This offset may indicate some evolution with the redshift, because Maiolino et al. (2008) and Troncoso et al. (2014) considered galaxies at higher redshifts (but not Maier et al. 2014). The mass-metallicity relation for high- $z$  galaxies is considerably flatter and is in better agreement with the relation for low- $z$  galaxies in the mass range  $\log M_{*}/M_{\odot} = 8.5 - 11$ , if only

data by Cullen et al. (2014) and Steidel et al. (2014) are considered.

#### 5.4 $\text{H}\beta$ luminosity - stellar mass relation

Finally, we consider the relation between the  $\text{H}\beta$  luminosity (or, equivalently, the SFR) and stellar mass, both corrected for extinction and aperture. At variance with relations discussed above this relation does not depend on the technique used for the determination of metallicity. Fig. 10a shows the relation between the extinction- and aperture-corrected  $\text{H}\beta$  luminosities (or SFRs) and stellar masses for the entire sample. The linear maximum-likelihood fit to the data is shown by a solid line. The sample is characterised by very high specific star formation rates  $\text{sSFR} = \text{SFR}/M_{*}$  ranging from  $\sim 0.1 \text{ Gyr}^{-1}$  to  $\sim 100 \text{ Gyr}^{-1}$  (dotted lines), which are among the highest for the local and high- $z$  star-forming galaxies. It is clearly seen that galaxies with younger starbursts (magenta symbols) have systematically higher  $\text{H}\beta$  luminosities, as compared to the galaxies with older starbursts (cyan symbols).

For comparison, in Fig. 10a we show data for high- $z$  star-forming galaxies by Cullen et al. (2014) and Steidel et al. (2014) (inside the box),  $\text{Ly}\alpha$ -emitting galaxies by Hagen et al. (2014) (stars), star-forming galaxies by Troncoso et al. (2014) (asterisks), star-forming galaxies with  $z \sim 4$  by Bouwens et al. (2012) (thick red solid line), star-forming galaxies with  $z \sim 5 - 6$  by Salmon et al. (2015) (thick yellow solid line), and galaxy candidates with  $z \sim 9 - 11$  by Coe et al. (2013) and Oesch et al. (2014) (large open dark-grey triangles). High- $z$  galaxies, including the highest redshift galaxy candidates, nicely follow the trend for low- $z$  galaxies with  $\text{EW}(\text{H}\beta) \geq 100\text{\AA}$  (magenta symbols), but are offset to higher  $L(\text{H}\beta)$  as compared to the rest of galaxies from our sample with presumably older starbursts (cyan symbols).

Reducing the  $\text{H}\beta$  luminosities (or, equivalently, SFRs) of galaxies from our sample to zero starburst age results in a much tighter relation in the redshift range  $0 < z < 1$  (magenta and cyan symbols in Fig. 10b). This is because the age correction for galaxies with  $\text{EW}(\text{H}\beta) \geq 100\text{\AA}$  is much smaller compared to that for the remaining galaxies of our sample. We note that the correction for the starburst age of the stellar mass is small because this parameter was obtained from the SED in the optical range, which is insensitive to age variations on the scale of several Myr. Therefore we did not introduce a correction for the stellar mass.

It is seen in Fig. 10b that the distributions of low- $z$

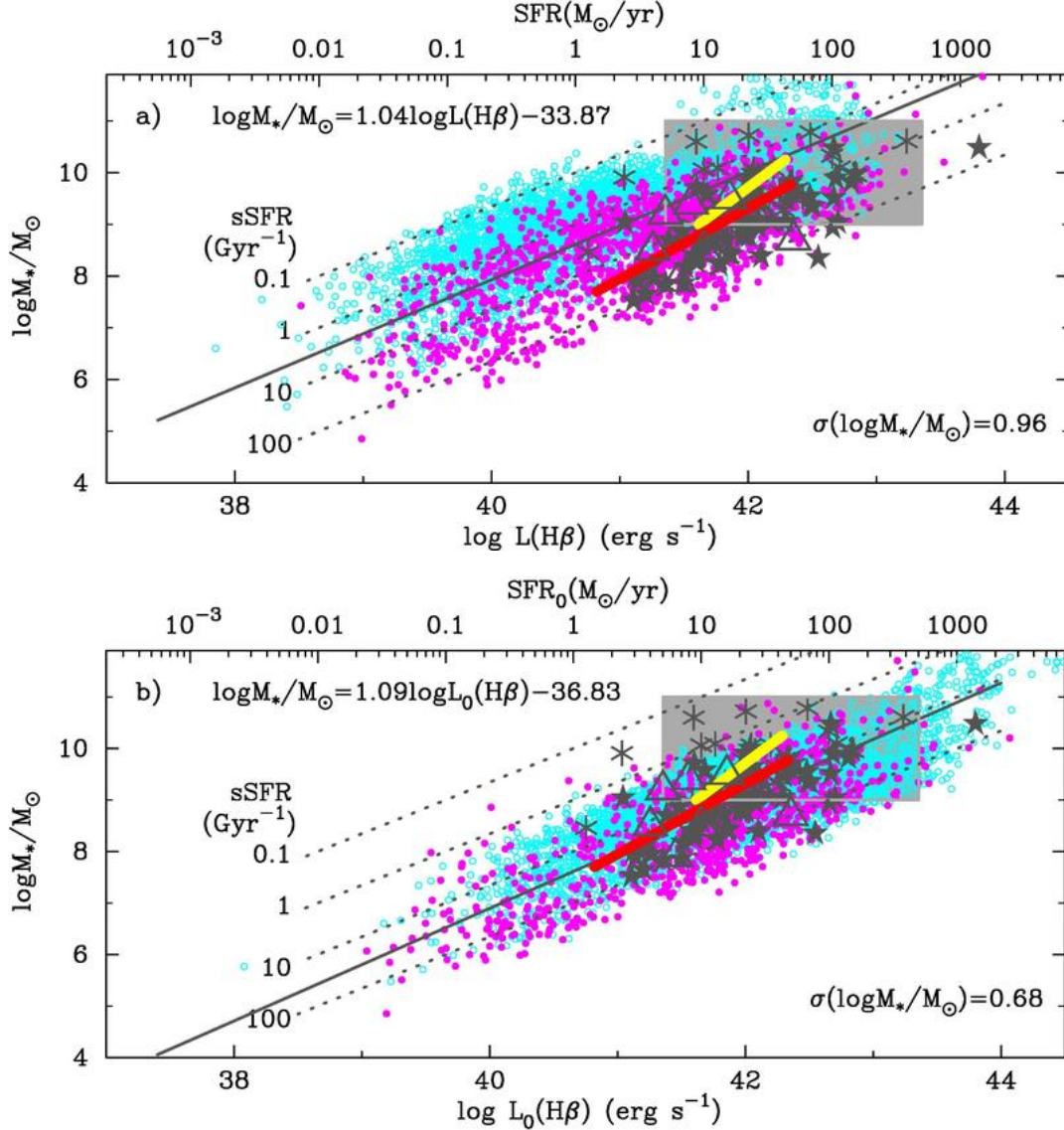


**Figure 10.** The stellar mass - H $\beta$  luminosity (or equivalently star-formation rate) relations for the entire sample. The extinction- and aperture-corrected H $\beta$  luminosities and stellar masses are shown in panel (a), while H $\beta$  luminosities are additionally reduced to zero starburst age in panel (b). Galaxies with the equivalent widths  $\text{EW}(\text{H}\beta) < 100\text{\AA}$  and  $\geq 100\text{\AA}$  are shown by the small cyan open circles and small magenta filled circles, respectively. Solid lines represent linear maximum-likelihood fits to all data. Constant specific star-formation rates (sSFR=SFR/ $M_*$ ) are shown by dotted lines and labelled by values in units of  $\text{Gyr}^{-1}$ . The location of star-forming galaxies with redshifts  $2.0 < z < 2.6$  by Steidel et al. (2014) and with  $z > 2$  by Cullen et al. (2014) is shown by a grey rectangle. Ly $\alpha$  emitting galaxies with redshifts  $1.9 < z < 3.6$  by Hagen et al. (2014) and star-forming galaxies with redshifts  $z \sim 3.4$  by Troncoso et al. (2014) are shown by dark-grey stars and asterisks, respectively. The relations for galaxies with  $z \sim 4$  by Bouwens et al. (2012) and for galaxies with  $z \sim 5 - 6$  by Salmon et al. (2015) are indicated by thick solid red and yellow lines, respectively. The galaxy candidates with  $z \sim 9 - 11$  by Coe et al. (2013) and Oesch et al. (2014) are shown by large open dark-grey triangles. The H $\beta$  luminosities of all high- $z$  galaxies in (b) are not reduced to zero starburst age.

and high- $z$  star-forming galaxies in the  $L_0(\text{H}\beta) - M_*/M_\odot$  plane are very similar, implying that the physical properties of these galaxies are similar as well. However, we note that H $\beta$  luminosities for high- $z$  galaxies are not corrected for the starburst age.

## 6 SUMMARY

We studied the relations between global parameters (absolute magnitudes, H $\beta$  luminosities, star-formation rates SFR,

stellar masses, and gas-phase oxygen abundances) of 5182 compact star-forming galaxies with high-excitation H II regions in the redshift range  $0 < z < 1$  selected from the SDSS DR7 and SDSS/BOSS DR10 surveys. These data were split into two samples, one is the  $T_e$  sample of 3607 galaxies, where the temperature-sensitive [O III] $\lambda 4363$  emission line was detected at the level better than  $1\sigma$  and the oxygen abundance was derived by the  $T_e$ -method, and the second sample consisting of the remaining galaxies, where the oxygen abundances were derived by strong-line methods. The

data for local galaxies were combined with respective literature data for high- $z$  galaxies (with  $2 \lesssim z \lesssim 3$ ) to detect a possible redshift evolution of global parameters in star-forming galaxy.

Our main results are as follows.

1. Using the  $T_e$  sample we analysed the oxygen abundances derived by the  $T_e$ -method and various strong-emission-line (SEL) methods used for the chemical abundance determination. We adopted strong-line methods, which are consistent with the  $T_e$ -method for high-excitation H II regions.

2. We analysed various relations between absolute magnitudes, H $\beta$  luminosities (or equivalently star-formation rates SFR), stellar masses, and oxygen abundances for our sample of low- $z$  compact star-forming galaxies in combination with the respective data for high- $z$  star-forming galaxies. We find good agreement between relations for low- $z$  and high- $z$  galaxies indicating very weak redshift evolution of global parameters and weak dependence of metallicity on SFR, contrary to results in some other studies. This finding emphasizes the universal character of relations for considered global parameters of compact star-forming galaxies with high-excitation H II regions at redshifts  $0 \lesssim z \lesssim 3$ . Furthermore, galaxy candidates at  $z \sim 9 - 11$  do not deviate from low- $z$  compact star-forming galaxies on the  $M_*$  – SFR diagram implying that universal relations between global galaxy parameters may be valid for galaxies at higher redshifts.

## ACKNOWLEDGEMENTS

Y.I.I., N.G.G. and K.J.F. are grateful to the staff of the Max Planck Institute for Radioastronomy (MPIfR) for their warm hospitality. Y.I.I. and N.G.G. acknowledge financial support by the MPIfR. Funding for the SDSS and SDSS-II has been provided by the Alfred P. Sloan Foundation, the Participating Institutions, the National Science Foundation, the U.S. Department of Energy, the National Aeronautics and Space Administration, the Japanese Monbukagakusho, the Max Planck Society, and the Higher Education Funding Council for England. The SDSS Web Site is <http://www.sdss.org/>. The SDSS is managed by the Astrophysical Research Consortium for the Participating Institutions. The Participating Institutions are the American Museum of Natural History, Astrophysical Institute Potsdam, University of Basel, University of Cambridge, Case Western Reserve University, University of Chicago, Drexel University, Fermilab, the Institute for Advanced Study, the Japan Participation Group, Johns Hopkins University, the Joint Institute for Nuclear Astrophysics, the Kavli Institute for Particle Astrophysics and Cosmology, the Korean Scientist Group, the Chinese Academy of Sciences (LAMOST), Los Alamos National Laboratory, the Max-Planck-Institute for Astronomy (MPIA), the Max-Planck-Institute for Astrophysics (MPA), New Mexico State University, Ohio State University, University of Pittsburgh, University of Portsmouth, Princeton University, the United States Naval Observatory, and the University of Washington. Funding for SDSS-III has been provided by the Alfred P. Sloan Foundation, the Participating Institutions, the National Science Foundation, and the U.S. Department of Energy Office of

Science. The SDSS-III web site is <http://www.sdss3.org/>. SDSS-III is managed by the Astrophysical Research Consortium for the Participating Institutions of the SDSS-III Collaboration including the University of Arizona, the Brazilian Participation Group, Brookhaven National Laboratory, Carnegie Mellon University, University of Florida, the French Participation Group, the German Participation Group, Harvard University, the Instituto de Astrofísica de Canarias, the Michigan State/Notre Dame/JINA Participation Group, Johns Hopkins University, Lawrence Berkeley National Laboratory, Max Planck Institute for Astrophysics, Max Planck Institute for Extraterrestrial Physics, New Mexico State University, New York University, Ohio State University, Pennsylvania State University, University of Portsmouth, Princeton University, the Spanish Participation Group, University of Tokyo, University of Utah, Vanderbilt University, University of Virginia, University of Washington, and Yale University.

## REFERENCES

- Abazajian K. N. et al., 2009, *ApJS*, 182, 543  
 Planck collaboration: Ade P. A. R., Aghanim N., Armitage-Caplan C., Arnaud M. et al., 2014, *A&A*, 571, A16  
 Ahn C. P. et al., 2014, *ApJS*, 211, 17  
 Aller L. H., 1984, *Physics of Thermal Gaseous Nebulae*. Dordrecht: Reidel  
 Alloin D., Collin-Souffrin S., Joly M., Vigroux L., 1979, *A&A*, 78, 200  
 Amorín R. O., Pérez-Montero E., Víchez J. M., 2010, *ApJ*, L128  
 Andrews B. H., Martini P., 2013, *ApJ*, 765, 140  
 Baldwin J. A., Phillips M. M., Terlevich R., 1981, *PASP*, 93, 5  
 Bouwens R. J., Illingworth G. D., Oesch P. A. et al., 2012, *ApJ*, 754, 82  
 Cardamone C. et al., 2009, *MNRAS*, 399, 1199  
 Cardelli J. A., Clayton G. C., Mathis J. S. 1989, *ApJ*, 345, 245  
 Charlot S., Longhetti M., 2001, *MNRAS*, 887  
 Coe D., Zitrin A., Carrasco M. et al., 2013, *ApJ*, 762, 32  
 Cullen F., Cirasuolo M., McLure R. J., Dunlop J. S., Bowler R. A. A., 2014, *MNRAS*, 440, 2300  
 Dawson K. S. et al., 2013, *AJ*, 145, 10  
 Dopita M. A., Sutherland R. S., Nicholls D. C., Kewley L. J., Fogt F. P. A., 2013, *ApJS*, 208, 10  
 Fioc M., Rocca-Volmerange B., 1997, *A&A*, 326, 950  
 Guseva N. G., Izotov Y. I., Thuan T. X., 2006, *ApJ*, 644, 890  
 Guseva N. G., Izotov Y. I., Papaderos P., Fricke K. J., 2007, *A&A*, 464, 885  
 Guseva N. G., Papaderos P., Meyer H. T., Izotov Y. I., Fricke K. J., 2009, *A&A*, 505, 63  
 Hagen A. et al., 2014, *ApJ*, 786, 59  
 Heckman T. M. et al., 2005, *ApJ*, 619, L35  
 Hoyos C., Koo D. C., Phillips A. C., Willmer C. N. A., Guhathakurta P., 2005, *ApJ*, 635, L21  
 Hunt L. K. et al., 2012, *MNRAS*, 427, 906  
 Izotov Y. I., Thuan T. X., Lipovetsky V. A., 1994, *ApJ*, 435, 647

- Izotov Y. I., Thuan T. X., & Lipovetsky V. A., 1997, *ApJS*, 108, 1
- Izotov Y. I., Stasińska G., Meynet G., Guseva N. G., Thuan T. X., 2006, *A&A*, 448, 955
- Izotov Y. I., Guseva N. G., Thuan T. X., 2011, *ApJ*, 728, 161
- Izotov Y. I., Guseva N. G., Fricke K. J., Henkel C., 2014a, *A&A*, 561, A33
- Izotov Y. I., Guseva N. G., Fricke K. J., Krügel E., Henkel C., 2014b, *A&A*, 570, A97
- Jaskot A. E., Oey M. S., 2014, *ApJ*, 791, L19
- Kakazu Y., Cowie L. L., Hu E. M., 2007, *ApJ*, 668, 853
- Kauffmann G., Heckman T. M., Tremonti C. et al., 2003, *MNRAS*, 346, 1055
- Kennicutt R. C., Jr., 1998, *Ann.Rev.Astron.Astrophys.*, 36, 189
- Kewley L. J., Dopita M. A., 2002, *ApJS*, 142, 35
- Kewley L. J., Ellison S. L., 2008, *ApJ*, 681, 1183
- Kobulnicky H. A., Kewley L. J., 2004, *ApJ*, 617, 240
- Lara-López M. A., Cepa J., Bongiovanni A. et al., 2010, *A&A*, 521, L53
- Lee H. et al., 2006, *ApJ*, 647, 970
- Leitherer C. et al., 1999, *ApJS*, 123, 3
- Maier C., Lilly S. J., Ziegler B. L., Pérez Montero E., Peng Y., Balestra I., 2014, *ApJ*, 792, 3
- Maiolino R. et al., 2008, *A&A*, 488, 463
- Manucci F., Cresci G., Maiolino R., Marconi A., Gnerucci A., 2010, *MNRAS*, 408, 2115
- Nicholls D. C., Dopita M. A., Sutherland R., Kewley L. J., Palay E., 2013, *ApJS*, 207, 21
- Oesch P. A., Bouwens R. J., Illingworth G. D. et al., 2014, *ApJ*, 786, 108
- Pagel B. E. J., Edmunds M. G., Blackwell D. E., Chun M. S., Smith G., 1979, *MNRAS*, 189, 95
- Palay E., Nahar S. N., Pradhan A. K., Eissner W., 2012, *MNRAS*, 423, L35
- Pettini M., Pagel B. E. J., 2004, *MNRAS*, 348, L59
- Pettini M., Shapley A. E., Steidel C. C. et al., 2001, *ApJ*, 554, 981
- Pilyugin L. S., 2001, *A&A*, 374, 412
- Pilyugin L. S., Thuan T. X., 2005, *ApJ*, 631, 231
- Pilyugin L. S., Vílchez J. M., Thuan T. X., 2010, *ApJ*, 720, 1738
- Refsdal S., Stabell R., de Lange F. G., 1967, *Mem. RAS*, 71, 143
- Salmon B., Papovich C., Finkelstein S. L. et al., 2015, *ApJ*, 799, 183
- Sanders R. L., Shapley A. E., Kriek M. et al., 2015, *ApJ*, 799, 138
- Smee S. A. et al., 2013, *AJ*, 146, 32
- Stasińska G., 2005, *A&A*, 434, 507
- Stasińska G., 2006, *A&A*, 454, L127
- Steidel C. S. et al., 2014, *ApJ*, 795, 165
- Tremonti C. et al., 2004, *ApJ*, 613, 898
- Troncoso P. et al., 2014, *A&A*, 563, A58
- York D. G. et al., 2000, *AJ*, 120, 1579
- Zahid H. J., Kewley L. J., Bresolin F., 2011, *ApJ*, 730, 137
- Zahid H. J., Bresolin F., Kewley L. J., Coil A. L., Davé R., 2012, *ApJ*, 750, 120
- Zahid H. J., Geller M. J., Kewley L. J., Hwang H. S., 2013, *ApJ*, 771, L19
- Zahid H. J. et al., 2014a, *ApJ*, 791, 130
- Zahid H. J. et al., 2014b, *ApJ*, 792, 75
- Zhao Y., Gao Y., Gu Q., 2010, *ApJ*, 710, 663

This paper has been typeset from a  $\text{\TeX}$ / $\text{\LaTeX}$  file prepared by the author.